Materials & Design 206 (2021) 109826

Contents lists available at ScienceDirect

Materials & Design

journal homepage: www.elsevier.com/locate/matdes

Property prediction and crack growth behavior in cold sprayed Cu deposits

Chunjie Huang [a,*], Mariia Arseenko [b], Lv Zhao [c], Yingchun Xie [d], Andreas Elsenberg [a], Wenya Li [e], Frank Gärtner [a], Aude Simar [b], Thomas Klassen [a]

[a] Materials Technology, Helmut-Schmidt-University/University of the Federal Armed Forces Hamburg, 22043 Hamburg, Germany
[b] Institute of Mechanics, Materials and Civil Engineering, UCLouvain, 1348 Louvain-la-Neuve, Belgium
[c] Department of Mechanics, Huazhong University of Science and Technology, 430074 Wuhan, China
[d] The Key Lab of Guangdong for Modern Surface Engineering Technology, National Engineering Laboratory for Modern Materials Surface Engineering Technology, Institute of New Materials, Guangdong Academy of Sciences, 510651 Guangzhou, China
[e] State Key Laboratory of Solidification Processing, Shaanxi Key Laboratory of Friction Welding Technologies, Northwestern Polytechnical University, 710072 Xi'an, China

HIGHLIGHTS

- Exact property prediction of Cu is derived for reaching threshold in using CS as AM.
- Post-spray annealing to gain properties similar to that of bulk material was studied.
- Macroscopic properties of CS Cu were correlated with micro-mechanics.
- Crack growth behaviors of CS Cu were discussed in as-sprayed and annealed states.

GRAPHICAL ABSTRACT

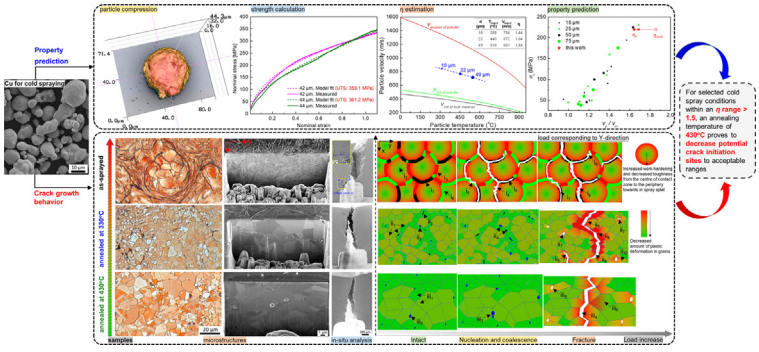

ARTICLE INFO

Article history:
Received 4 December 2020
Revised 25 April 2021
Accepted 12 May 2021
Available online 13 May 2021

Keywords:
Cold spraying (CS)
Annealing
Strength-ductility
Crack growth behavior
In-situ SEM tensile testing

ABSTRACT

Low ductility of metallic deposits manufactured by cold spraying (CS) impedes potential mechanical performances in industrial applications. Through appropriate annealing treatment, the amount of both, non-bonded interfaces and work hardening promoted dislocations during CS can be significantly reduced. Consequently, the annealed samples exhibit higher strength and fracture strain than the as-deposited ones. Cu was selected as a reliable material for CS. To correlate Cu deposit strength with primary process parameters and material properties, the Cu powder strength was assessed. Crack characterization of Cu deposits was performed by in-situ microscopic observations during tensile testing. The direct observation of crack initiation, growth and final fracture allows revealing failure mechanisms. The in-situ tests allow distinguishing the effects of reduced initial defect sizes due to annealing and improved ductility in the vicinity of initial defects on possible crack growth and part failure. Considering the necessary compromise between strength, uniform elongation, ductility and microhardness, a post-spraying annealing process is desirable for CSed Cu deposits. The identification of macroscopic and micro-mechanical properties attained under respective process parameters and influences of annealing processes therefore allow identifying solutions for improvements of CSed deposits for load-carrying applications, which is a prerequisite for using CS as additive manufacturing technique.

* Corresponding author.
E-mail address: huangc@hsu-hh.de (C. Huang).

https://doi.org/10.1016/j.matdes.2021.109826
0264-1275/

1. Introduction

1.1. Context

Additive manufacturing (AM: such as selective laser sintering/melting, electron beam melting) based on layer-by layer fusion build-up, attracts increasing attention for structural design. AM is more flexible and causes less material waste than subtractive manufacturing techniques [1]. Actual applications are promoted for automotive, aerospace and biomedical industries [1,2]. However, the state of the art also underlines that high-temperature AM processes are generally associated with some disadvantages and limited performance due to porosity and cracks, especially in manufacturing materials showing high reflectivity and thermal conductivity, such as Cu, Al and Ag alloys [3].

In contrast to the high-temperature AM techniques, cold spraying (CS) as a solid-state powder deposition process, has developed from a traditional coating method to a new-type AM approach. It can alleviate problems related to the high temperature processing of metallic materials, such as oxidation, decomposition and phase transformation, as well as grain growth of the sprayed deposits during build-up [4–8]. As an effective method to produce high quality metallic deposits, CS has attracted substantial attention as AM or repair technique for components of advanced metallic structural materials [4–10]. In addition, it is a promising method to fabricate high-performance bulk materials that can only be synthesized as powder [8]. Among metallic materials, Cu combines both high plasticity and excellent electrical/thermal conductivity. Thus, the interest for CS Cu has increased in both academic [9,11–15] and industrial [5,16] investigations. As compared to bulk material, cold sprayed deposits reach electrical conductivities of up to 95% [11] and nearly similar strengths [12,13]. However, so far, the ductility of CS Cu is much lower than that of the bulk Cu alloys [6].

Therefore, in order to fulfill criteria for CS of Cu to serve in structural applications, deeper knowledge on associated failure mechanisms is needed. Subsequent annealing can be used to tune deposit strengths, but often fails to reach the required ductility by completely healing out possibly over-critical crack nuclei. Thus, despite widely explored properties of CS Cu-deposits, there is still a need for a better understanding of the role of inherent defects on crack formation and propagation and their hindering by annealing. This paper focuses on the influence of initial powder strength on the deposit quality parameter η and possible correlations with the micro and macroscopic mechanics of obtained deposits in as sprayed and annealed states. This will allow to define prerequisites to reach bulk-like deposit mechanical performances. The mechanism is revealed by in-situ SEM analyses during tensile testing. The knowledge on deposit quality prediction and counter measures against crack growth mechanisms may also be transposable to other CS-AM materials.

1.2. Correlation between deposit quality parameter- η and deposit cohesive strength

Bonding in CS occurs if the velocity of the impact particle v_p is higher than the corresponding critical velocity v_{cr}. For different particle sizes, the relationship between the impact velocity v_p and the deposit cohesive strength σ_c of Cu deposits was studied in Ref. [11]. It was shown that the variation of σ_c with v_p strongly depends on particle size. Assadi et al. [17] found that there exists a unique correlation between the cohesive strength σ_c and the velocity ratio ηin spite of the particle size distribution or spraying conditions. This, the quality parameter η is defined as the ratio of v_p to v_{cr}. σ_c was plotted against the quality parameter η, which was demonstrated to be identical for all of the examined powders. That is to say that, the deposit properties, like σ_c, can be linked to the parametric expression of η [8,17]. However, several questions naturally arise with respect to the above correlation: i) How accurately is the calculation of v_{cr}, which influences the value of η? ii) How precise are calculations of v_p under slight variation of nozzle shape and other influences by using different types of CS systems. (iii) What influences do different Cu powder shapes have?

1.3. Ductility in CS Cu deposits

Although a considerable deposit strength can be achieved by increasing v_p with optimum process parameters, the ductility remains low, e.g., by shifting process gas from N_2 to He, the ultimate tensile strength (UTS) was improved from 77 MPa to 454 MPa and the elongation at failure was increased from <0.1% to 2.5% [13]. As compared to the elongation at fracture of annealed bulk copper (49.7% [13]), this ductility of 2.5% as achieved by the selection of He as process gas is still far too low. Indeed, CS Cu deposits show some shortcomings, which cannot be eliminated through optimizing the spraying parameters. For example, non-bonded interfaces and highly work hardened areas in the vicinity of the interfaces generally lead to a low ductility [8,13]. In addition, internal deposit microstructures are highly non-uniform and anisotropic [14,15]. However, the elongation to fracture of Cu deposits can be greater than 3%, even reaching 29% using selected spraying conditions or treatments [18].

Regardless of AM techniques, one major concern is whether the process can produce parts with sufficiently high strength and ductility for industrial applications [1,2,4,5,8]. Often, in practice, materials deposition by CS is followed by a post-spraying annealing process to improve ductility and to gain better damage tolerance. Although the minimization in microstructural anisotropy and the improvement on ductilization of CS Cu deposits by post annealing has been widely reported [12–15,19,20], the direct influence of annealing treatment and related microstructural changes on crack initiation and propagation have not been reported.

By fractographic observations of as sprayed conditions and different annealing states (200, 400 and 600 °C for 1 h) of CS Cu deposits, Gärtner et al. [13] indicated that failure at particle–particle interfaces is less prominent after using higher annealing temperatures. In addition, Yu et al. [19] and Singh et al. [20] showed that an initially cleavage-type fracture changes to a ductile one by deposit annealing (350 °C for 1 h and 450 °C for 1 h, respectively). Fractographic details revealed that, the as-sprayed deposit showed multiple failure at particle boundaries while the crack growth can be restricted after heat-treatment. However, a direct link between the enhancement of mechanical performance such as strength and fracture strain and the decease of initial crack length (non-bonded interfaces) or other defect size (like voids) was not clearly revealed in that work. So far, associated crack growth mechanisms have not been substantially addressed and the effects of different annealing temperatures on damage tolerance and crack propagation remain unclear.

1.4. Aim of this work

In order to obtain a more realistic σ_c-η correlation and to shed light on details of the fracture mechanisms, the micro-mechanical properties of Cu particles were analyzed by particle compression testing. CS parameters with nitrogen as process gas were deliberately set to a rather high regime to limit sizes and amounts of non-bonded internal interfaces. In addition to investigations of as-sprayed state, microstructures are modified by using two selected annealing temperatures (330 and 430 °C), that were reported to show significantly different influences on strength

and ductility [12]. In-situ SEM tensile testing of these different states was conducted to investigate the elongation at fracture and reveal details of crack propagation behaviors by using the notch-free and pre-notched samples, respectively. The combination of different macroscopic analyses and detailed observations of in-situ crack propagation should allow a more general understanding on the interplay between global deposit properties and associated micro-mechanics.

2. Materials and methods

2.1. Initial powder

Fig. 1a and 1b show the respective morphologies of the surface and the unetched cross-sections of high purity Cu powder (>99.9%) used in these sets of experiments, as observed by scanning electron microscopy (SEM, Quanta 650, FEI, Czech Republic). The particle size distribution was measured by laser scattering using a particle sizer type (LA-910, Horiba, Japan). The powder sizes were identified as D-values of D10, D50 and D90 of 10, 22 and 49 μm, respectively, see Fig. 1c. The grain size of Cu particle was analyzed on etched particle cross-sections by SEM (Fig. 1d). The grain size varies from a few micrometers to a maximum of 15 μm (at least ten particles investigated). No pores or oxides inside the particles were observed on the unetched and the etched cross-sections (Fig. 1b and 1d). A top view of a 44 μm Cu particle obtained by confocal microscopy (3D Laser Scanning Microscope VK-X200 series, KEYENCE, Germany) is shown in Fig. 1e.

2.2. Particle compression test

The strength of powder particles is usually higher than that of the respective cast bulk materials due to finer grain sizes as obtained under the high-cooling rate of their production process by atomization [21]. In consequence, v_{cr} for deposit formation are usually higher than estimated on basis of bulk material data. Aiming to calculate more realistic v_{cr} for bonding and the deposit quality parameters η as measure of possible deposit strength, the particle strength should be evaluated and used as input data in calculations.

The particle strength is determined using a powder compression method. The compression and deformation steps were schematically described in Refs. [21,22]. This test was conducted using a modified microindenter (ZHU2.5/Z2.5, Zwick/Roell Instruments, Germany) with a flat indentation tip of 200 μm diameter. Prior to compression test, the particle shape and size were analyzed using confocal microscopy (3D Laser Scanning Microscope, VK-X200 series, KEYENCE GmbH, Germany). The obtained force–displacement curves were then transformed into the nominal stress–strain curves using an in-house program to determine the particle strength. Ten particles were tested. Detailed information for UTS calculation is provided in Refs. [21,22].

2.3. Parametric η estimate

Prior to spraying, the software KSS (Kinetic Spray Solutions, Germany) [23] was employed to predict the particle velocities and temperatures as impact conditions under the selected spraying parameters as well as temperature dependent critical velocities. The basic principles of this software have been described by Schmidt et al. [11] and Assadi et al. [17]. In the present case, the critical velocities and the thus related quality parameters η were evaluated by measuring the particle strengths and use these as input data (refer to section 2.2). The bulk Cu strength extracted from Ref. [21] is used for comparison purposes.

2.4. Cold spraying, sample preparation and annealing

The deposit was manufactured with a commercial cold spraying system of type PCS-800 designed by Plasma Giken, Japan by using a commercial De-Laval type nozzle. Nitrogen was used as process and carrier gas. A gas inlet temperature of 800 °C and a stagnation pressure of 4 MPa were identified as the optimum spraying parameters [12]. In addition, the line traverse speed and the powder

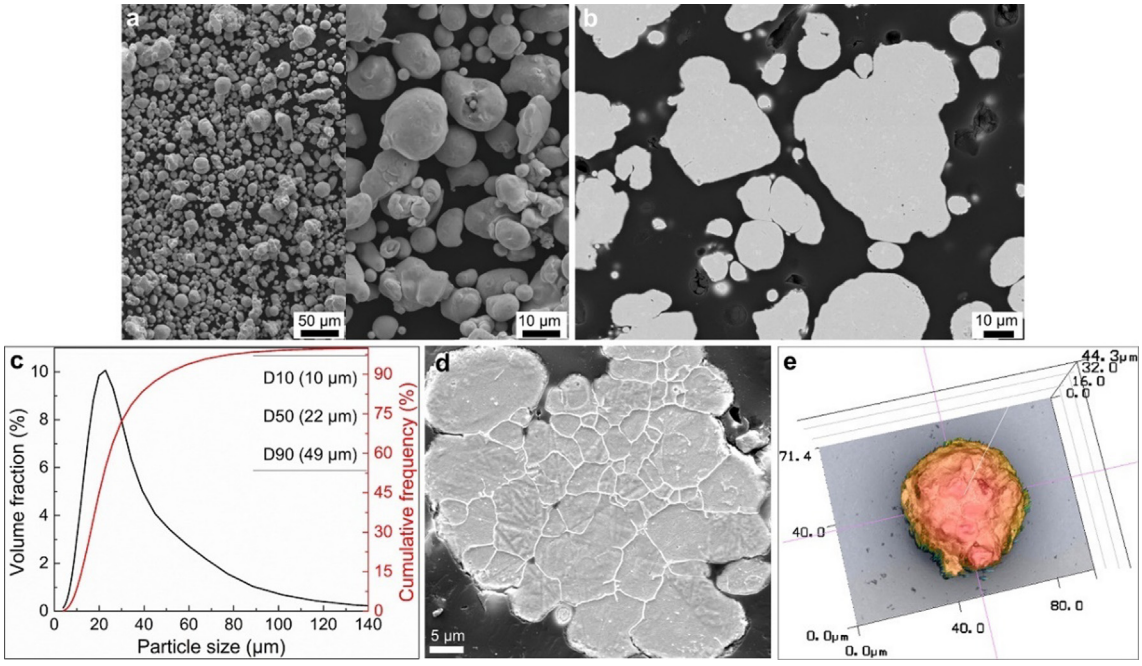

Fig. 1. Morphologies, microstructures and sizes of the as-received Cu powder (powder source and supplier may be not disclosed). (a) Powder morphologies as obtained by SEM in (a) top view (left: low magnification, right: high magnification), and (b) as cross-section. (c) Particle size distribution. (d) Powder microstructure as revealed by a SEM micrograph of a cross-section after etching. (e) Top view of a 44 μm Cu particle observed by confocal microscopy.

feeder rotational speed were fixed at 200 mm/s and 8 rpm, respectively. The stand-off distance and the distance between spray lines were set up at 30 mm and 1 mm, respectively. An Al alloy plate was used as substrate, and an at least 1.5 mm thick deposit was built in order to extract samples for ex-situ and in-situ tensile testing.

The samples for mechanical testing (Fig. 2b) were extracted from the deposit/substrate by electrical discharge machining (EDM) parallel to the spraying gun traversing direction. The deposits were separated from the substrate by polishing them to a thickness of 1 mm. Aiming for the full recrystallization temperature, i.e. larger than 400 °C in Cu deposits [12,24]), a lower (330 °C) and a higher (430 °C) temperature for annealing in vacuum for 4 h was selected to study influences with the induced difference in diffusion lengths. The annealing treatment was performed in a high-vacuum oven type VHT8/18-KE from Nabertherm (Germany) under a vacuum of 2×10^{-5} bar, and using N_2 cooling with a cooling rate of 10 °C/min.

2.5. Characterization

2.5.1. Microstructural analysis

The samples of as-sprayed and annealed deposits for optical microscopy (OM, DMRM Leica, Germany) were first polished to a mirror-like surface and then etched with Klemm solution (100 ml cold saturated $Na_2S_2O_3$ + 40 g $K_2S_2O_5$) for 15 s. As grain boundary etchant, this revealed the microstructures of deformed and recrystallized grains. Grain size analysis and locally non bonded areas were analyzed and quantified by an image processing software (ImageJ 1.51a, NIH, USA).

The as-sprayed samples and the specimens annealed at 330 and 430 °C were further analyzed using a dual-beam focused ion beam (FIB) instrument (FEI Helios NanoLab DualBeam, ThermoFisher Scientific, USA). FIB extraction was performed for selective analyses of particle–particle interfaces. Microstructural analysis of selected areas by FIB preparation was performed by a high-resolution SEM (HR-SEM) of type Helios G4 UC from FEI-Thermo Fisher Scientific, USA. This allows for a detailed identification of grains in different crystal orientations and defects like pores, oxides and cracks.

2.5.2. Mechanical tests

The mechanical tests (detailed geometry and size of sample are presented in Fig. 2a) were performed using a micro-tensile equipment (Gatan micro-test tensile stage, MT10187, DEBEN, UK). Global mechanical properties, such as strength and fracture strain, were assessed on notch-free samples using ex-situ tensile testing. Loading was applied parallel to the spraying lines at a rate of 0.1 mm/min (Fig. 2c). The engineering stress as a function of global extension may then be plotted. The true strain of the samples denoted by the macroscopic fracture strain, was computed from analysis of the surface areas before and after fracture using ex-situ tensile testing. For in-situ SEM tensile testing, the elongation at fracture was estimated by image analysis (FEGSEM Ultra 55, CARL ZEISS AG, Germany) at initial and final fracture states. After failure, the fracture surface morphologies were examined by SEM. The microhardness measurements were performed on the polished surface (XY plane) by a Vickers indenter with a load of 300 g ($HV_{0.3}$, Zwick/Roell Instruments, Germany) using minimum ten indents ensuring sufficiently good statistics.

In order to investigate details of the fracture mechanisms, in-situ SEM tensile testing was performed on single edge pre-notched samples. This allows to monitor the correlation between microstructures, local deformation and crack propagation. Pre-notching is needed for pre-defining the location of cracking and allow for pre-set high magnification analyses. The position and dimension of the notch introduced by EDM are provided in Fig. 2-d-e. The observed surface (XY plane) was priory polished with oxide polishing suspension (OPS) and chemically etched for examining the microstructural evolution during tensile loading.

3. Results

3.1. Particle impact conditions

3.1.1. Particle strength

The mechanical properties of particles have a major influence on the critical velocity in CS. Within the examined range of 13–87 μm, the Cu particle strength should not be size-dependent

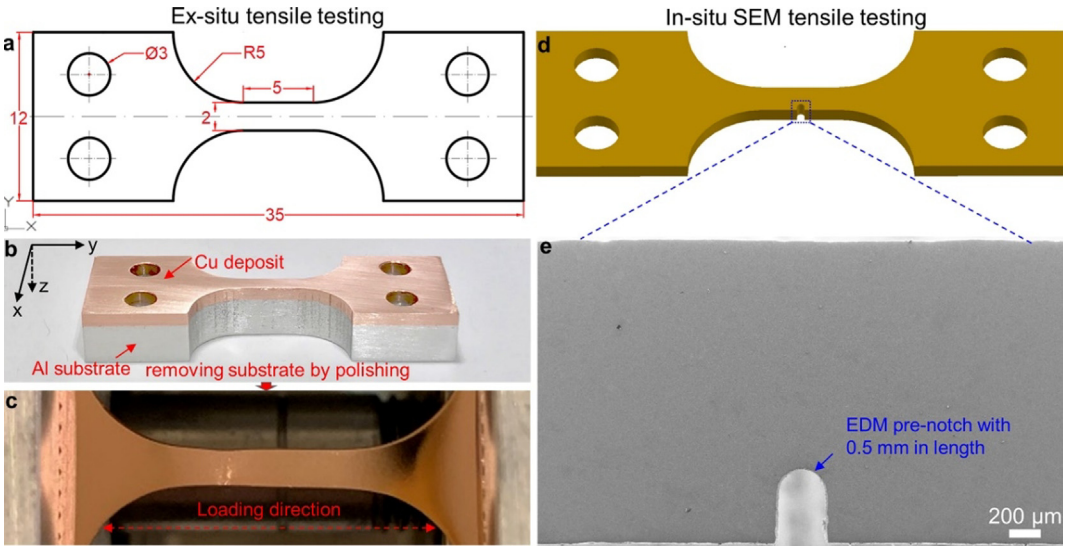

Fig. 2. a) Geometry and dimensions of the ex-situ and in-situ mechanical test samples. b) Photographic image of EDM machined sample, the particle deposition direction corresponding to the Z-axis direction, the Y-axis corresponding to the traverse direction of deposition spraying lines. c) Photo of an ex-situ tensile sample (annealed at 430 °C) during loading process before final fracture. At this loading stage, an onset of necking can be observed. d) Pre-notch extraction position in the in-situ tensile samples, and e) SEM image of EDM pre-notched sample where the substrate is removed by polishing before testing.

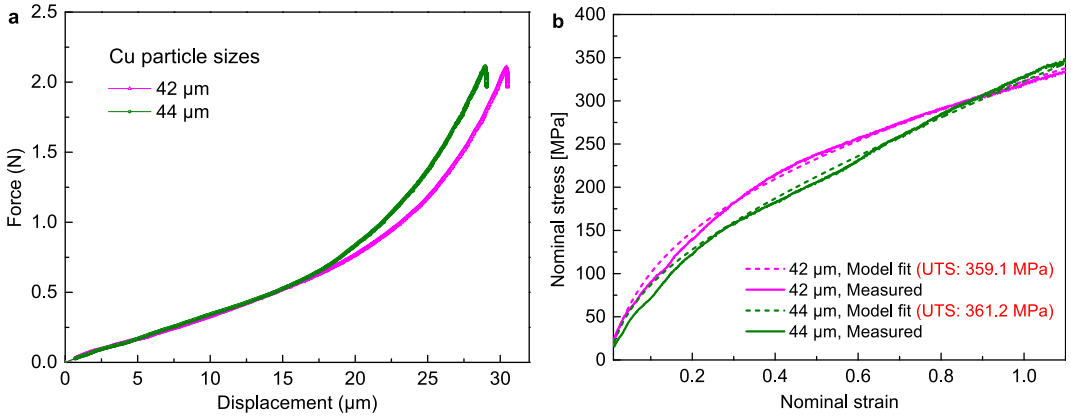

Fig. 3. Deformation during particle compression test. (a) Raw force–displacement curves. (b) Corresponding nominal stress strain curves as converted from the raw force–displacement data of (a) using the method described in Ref. [21]. (For interpretation of the color codes in this figure legend, the reader is referred to the Web version of this article).

[21]. As an example of particle deformation, Fig. 3a shows the raw force–displacement curves under compression of two selected, rather spherical Cu particles with similar diameters of 42 μm and 44 μm. The deformation behavior of both particles is similar, showing that a compressive displacement of nearly 30 μm is attained at the selected maximum force (2 N).

The raw data from the particle compression testing were converted to nominal stress–strain curves given in Fig. 3b using the method described in [21,22] (see also Section 2.2). The ultimate tensile strength of the micro-particles was evaluated from the stress–strain curve. For the selected examples with sizes of 42 μm and 44 μm, the UTS was calculated as 361 MPa and 359 MPa, respectively. These values are rather similar to the UTS (360 MPa) of the Cu particles with sizes of 25 μm, see Ref. [21]. The good agreement demonstrates that powders of the actual feedstock should show similar microstructures and purity. However, the experimentally obtained powder strength is significantly higher than that of bulk oxygen free high conductivity (OFHC) Cu material (230 MPa in Ref. [13]). In the following calculations (section 3.1.2), a mean UTS value of 361 MPa is used for the estimation of the critical velocity v_{cr} and the deposit quality parameter η.

3.1.2. Particle impact conditions

Fig. 4a shows the window of deposition (WoD, see Ref. [8]) in order to provide an overview of the influence of the Cu particle size (see Section 2.1) in the cold spray process on their individual impact conditions in comparison to critical velocities (v_{cr}). Table 1 summarizes the corresponding impact conditions and the deposit quality parameters η evaluated for the spraying parameter set provided in Section 2.4.

Fig. 4a shows that the particle impact conditions depend on its sizes. Increasing the particle size from 10 to 49 μm leads to an increase in impact temperature from 288 to 539 °C and to a decrease in particle impact velocity from 754 to 601 m/s, respectively. As illustrated by the superimposed plots in Fig. 4a, the critical velocities calculated on basis of the aforementioned particle strength (as denoted by green line) is higher than that obtained by using the UTS of soft annealed bulk Cu (Ref. [13], as denoted by the grey line). This demonstrates that an inappropriate estimate of particle strength can lead to an underestimation of v_{cr}, and ultimately lead to an overestimation of the quality parameter η.

Fig. 4b shows the development of gas and particle temperatures along the axial path through the nozzle. With the given powder injection up-stream nozzle throat, the small and medium size of particles (10 μm, 22 μm) nearly reach the gas temperature through heating within the pre-chamber (Fig. 4b). However, larger particles of 49 μm in size are only heated to about 650 °C before passing through the nozzle throat (0 mm on the x-axis). Downstream of the nozzle throat, the expanding gas stream quickly cools down by expansion. In consequence, the particle temperatures also drop.

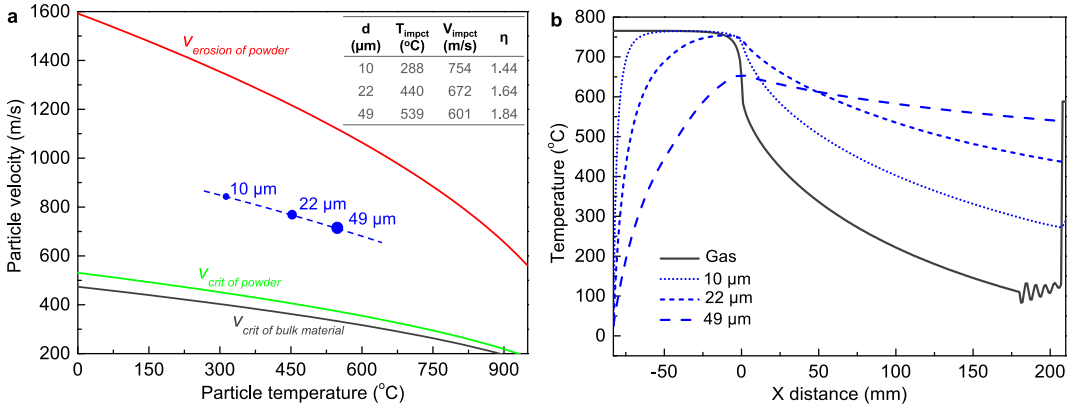

Fig. 4. (a) Impact conditions for CS Cu particles (D10 = 10 μm, D50 = 22 μm, D90 = 49 μm) using N_2 as process gas at p_{gas} = 4 MPa, T_{gas} = 800 °C and window of deposition (WoD) as calculated by KSS. The two bottom curves (green and grey lines) define the critical velocities calculated on basis of the respective strength of Cu particle and bulk material (229 MPa in Ref. [13]). The upper red curve represents the erosion velocities. Impact conditions and quality parameter η for the particle sizes are provided in the inserted table. (b) Gas and particle temperatures along the axial path through the nozzle. (For interpretation of the references to color in this figure legend, the reader is referred to the web version of this article.)

Table 1
Impact conditions of Cu particles at P_{gas} = 4 MPa, T_{gas} = 800 °C and respective η values, as obtained by KSS software.

v_p	T_p	v_{p_cr}	v_{bulk_cr}	η_p	η_{bulk}
674 m/s	429 °C	416 m/s	364 m/s	1.64	1.85

However, due to their higher thermal inertia, the larger particles retain more heat and thus maintain higher temperatures for longer traveling distances than the smaller ones.

3.2. Deposit microstructures

3.2.1. As-sprayed state of deposits

Fig. 5a-c show the etched microstructures observed by OM for the cross-sectional view (YZ plane) of the as-sprayed sample. Due to the plastic deformation of solid particles during impact, the microstructure shows highly flattened spray splats. The deposit shows no porosity. Most of the internal interfaces are well bonded (indicated by green arrows in Fig. 5c). Such well bonded interfaces are due to the shear instabilities under thermal softening owing to the high impact velocity (674 m/s, Table 1) of Cu particles during CS [8]. The ratios of the well-bonded interfaces to the overall interface areas [25] in the sprayed materials are consistent with the impact conditions estimated by the spraying parameter. Deposited particles are highly work hardened. Respective consequences on the mechanical properties and crack growth behaviors of as-sprayed deposit will be discussed in Section 3.4.1.

Looking at the etched sample surface (XY plane), see Fig. 5d-f, a heterogeneous grain microstructure induced by the inhomogeneous deformation can be observed. Highly localized deformation areas (red arrow in Fig. 5e), non-bonded particle–particle interfaces (black arrows in Fig. 5e) and specific grain morphologies and grain boundary arrangements (green arrow in Fig. 5e) inside the deposited particle can be observed. At higher magnification, as shown in Fig. 5f (corresponding to the black dashed rectangle region in Fig. 5e), three typical microstructural features associated with the deformation can be distinguished: 1) At the splat center (as indicated by green dashed line), grains with minor deformation and refinement show similar grain sizes as the as-received powder (compare Fig. 1d); 2) Near the particle–particle interface, grain refinement occurs due to dynamic recrystallization [25,26], as circled by the blue dotted line; 3) In the vicinity of highly work-hardened areas, recrystallization twins (see inset in Fig. 5f) are formed due to the local temperature rise induced by the deformation under impact [26].

3.2.2. Annealed states of deposits

The strain to failure of as-sprayed deposits is rather low due to the highly work-hardened state of the material and some non-bonded internal interfaces remaining between the spray splats. Annealing, can lead to microstructure rearrangement from the deformed state through recovery and diffusion-driven processes such as recrystallization and spheroidization of planar inter-particle defects, similar to a sintering process [13]. Therefore, the ductility is expected to be greatly improved by post-spraying heat-treatment. Two different annealing temperatures with distinct influences on diffusion and recrystallization are used to investigate the microstructural evolution of the as-sprayed deposits.

Fig. 6 presents the surface microstructures for deposits annealed at 330 and 430 °C for four hours. Different features are revealed after etching. At the lower annealing temperature of 330 °C, recrystallization prematurely occurs in the heavily deformed areas, which results in the formation of new small strain-free grains as well as annealing twins. However, some of the original particle–particle interfaces are still visible, by a few non-bonded interfaces still being present (black arrows in Fig. 6a). When the annealing temperature is increased to 430 °C (Fig. 6d-f), original splat boundaries cannot be identified anymore. Grain growth becomes more prominent and non-bonded interfaces diminish. This indicates that annealing at 430 °C is more efficient

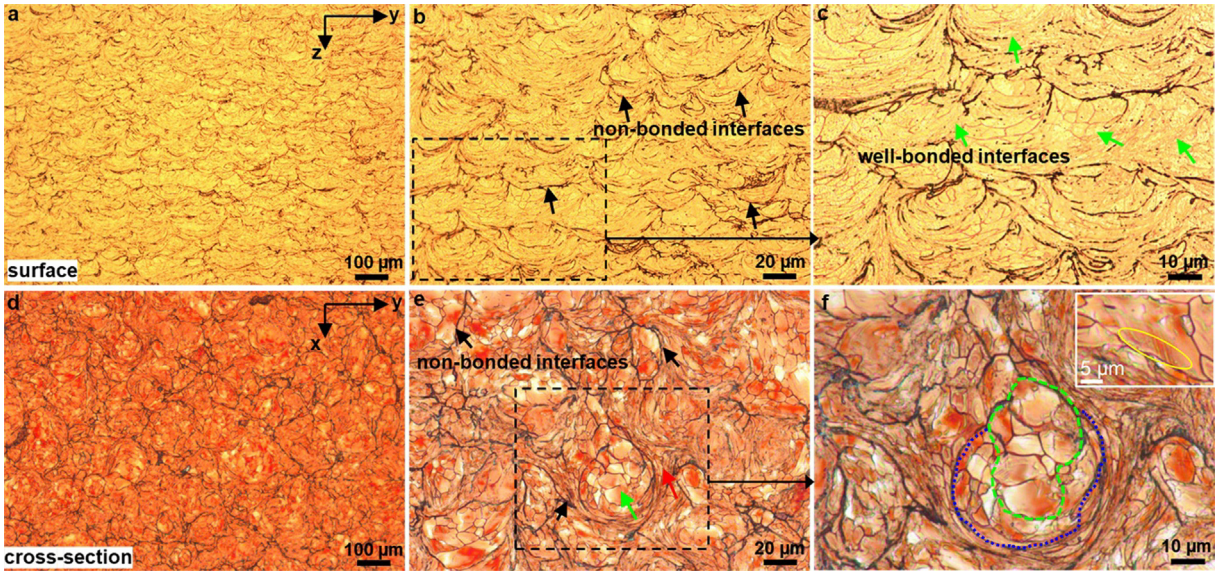

Fig. 5. Deposit microstructures as revealed by optical microscopy on of as-sprayed Cu samples. (a-c) show cross-sectional views (YZ plane, Fig. 2) and (d-f) show surface views (XY plane, Fig. 2). The details of (c) and (f) correspond to the black dashed rectangles in (b) and (e). The green arrows in (c) highlight well-bonded interfaces. The red, black and green arrows in (e), see zoom in (f) indicate the highly localized deformation area, the non-bonded particle–particle interface and less deformed grains within the particle, respectively. The yellow circle in the inset of Fig. f highlights twins. (For interpretation of the references to color in this figure legend, the reader is referred to the web version of this article.)

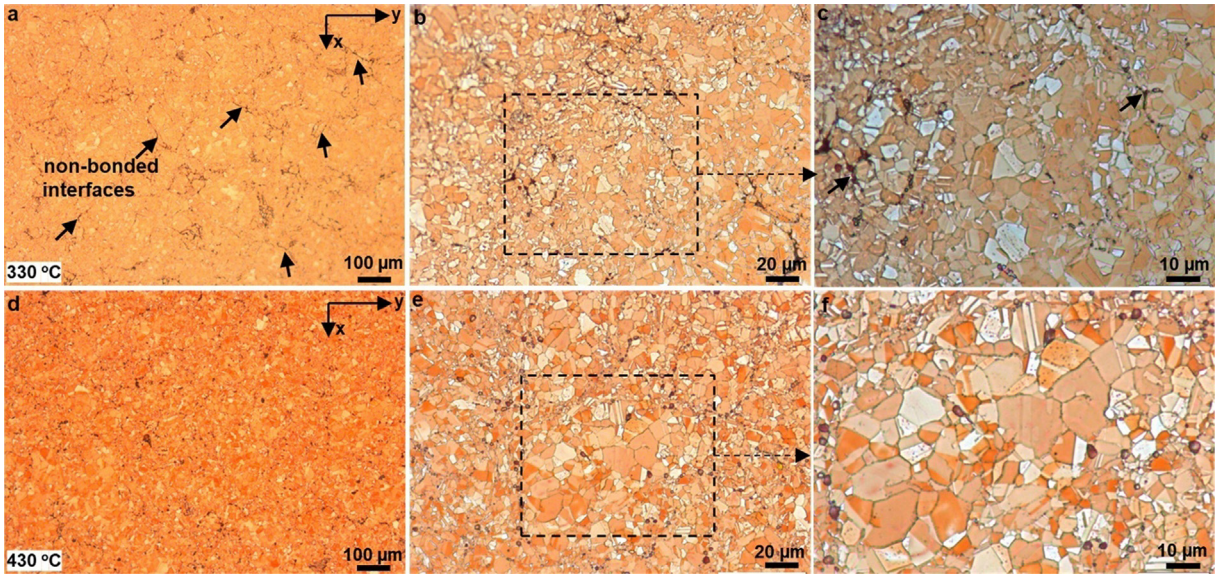

Fig. 6. Microstructures of annealed Cu deposits. (a-c) and (d-f) surface views (XY plane) after annealing at 330 °C and 430 °C for 4 h, respectively. (c and f) show details at a higher magnification (corresponding to the black dashed rectangles in Fig. b and e). The black arrows in Fig. a and c indicate non-bonded interfaces.

to cause recrystallization and grain growth as well as to shrink defects by surface diffusion along non-bonded interfaces, here originally present as micro-cracks.

3.2.3. Microstructural details

More information and details on defects, like porosity and heterogeneous grain structures, are obtained by applying FIB and HR-SEM of the as-sprayed deposit (Fig. 7a-b). The analysis reveals pre-existing micro-cracks and significant grain refinement at the respective nonbonded and well-bonded particle–particle interface, see the black and green arrows in Fig. 7a, respectively. Elongated subgrains are formed in the region near to the interface due to the accumulation of dislocations from the high-velocity impact [19]. Porosity (Fig. 7b), grain refinement at interface (Fig. 7a) and non-bonded interface (Fig. 7a) have a combined effect on possible fracture of such cold-sprayed Cu deposits. After annealing at 330 °C, recrystallization is most prominently observed at the internal interface (Fig. 7c-d), as revealed by the small grain size and the different crystal orientation contrast of the neighboring grains. Some non-bonded interfaces (black arrows in Fig. 7c) are found to be partially healed out by diffusion (sintering effect), as indicated by red arrows. The free volume of micro-cracks present in the non-bonded interfaces between particle splats seems to be transformed into spheroidized voids (blue arrows), minimizing surface energy (Fig. 7c). In addition, the elimination of high dislocation densities and grain growth (from the internal interfaces towards particle center) results in microstructure homogenization. This lower annealing temperature already reduces the amount of defects and can enhance mechanical properties of the deposit. At high magnification (Fig. 7d), few trapped oxides (white arrows)

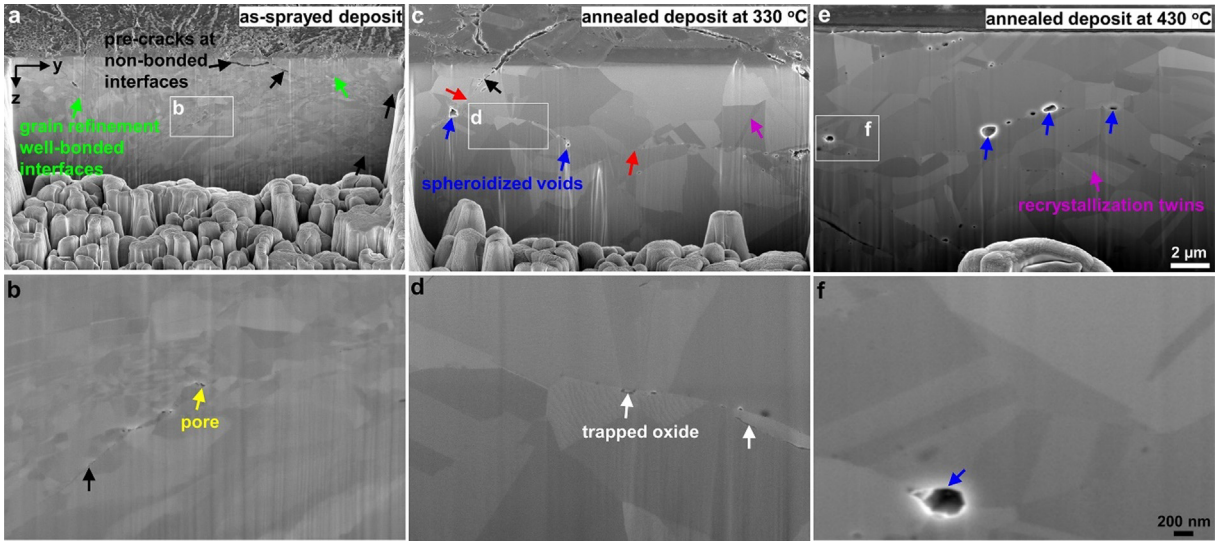

Fig. 7. Microstructural details of the as sprayed and the annealed deposits as observed by FIB and SEM. Fig. b, d and f correspond to the white boxes in (a, c and e). (a and b) As-sprayed deposit. (c and d) and (e and f) Deposits annealed at 330 °C and 430 °C, respectively. (a, c and e) General appearances after ion milling. The inserts in Fig. 7 show, black arrows: non-bonded interfaces, green arrows: grain refinement at well-bonded interfaces, red arrows: healed out interfaces after annealing, yellow arrow: pore at the non-bonded interface, blue arrows: spheroidized voids, purple arrows: recrystallization twins and white arrows: trapped oxide remnants. (For interpretation of the references to color in this figure legend, the reader is referred to the web version of this article.)

can be found at internal interfaces [25], probably as remnants from material jets. When annealing temperature is increased to 430 °C, well above the recrystallization temperature (Fig. 7e-f), most of the non-bonded interfaces are eliminated while spheroidized voids and grain growth become more prominent. For the annealed deposits, recrystallization twins are observed, as shown by purple arrows in Fig. 7c and e.

3.3. Mechanical deposit performance

3.3.1. Strength and ductility

In order to quantify the strength and fracture strain of as-sprayed and annealed samples, ex-situ tensile tests on the notch-free samples were performed. The tensile engineering stress versus global displacement curves until fracture are presented in Fig. 8a. The curves for the annealed states show uniform deformation, while the as-sprayed deposit fractures without any plastic deformation. These plots confirm the significant influences of annealing on the mechanical behavior of cold-sprayed deposits, in agreement to literature [12,13,20].

The tensile tests data of as-sprayed and annealed states (ultimate tensile strength, the elongation at fracture and the fracture strain) are determined as mean values from two tensile measurements and are summarized in Table 2. Assuming constant volume during plasticity, the true strain at fracture, $\varepsilon_f = \ln (A_0 / A_f)$ is determined on basis of the initial (A_0) and final (A_f) cross-section areas of the fractured samples. The analyses of fracture areas were performed at the smallest sample widths at fracture using SEM analysis, as shown in Fig. 8b. When compared to the as-sprayed sample, the annealing at 330 °C results in the increases of both, UTS and elongation at fracture. For an annealing temperature of 430 °C, the elongation at fracture increases but the strength slightly decreases. However, the yield strength of the as sprayed deposit is higher than that of the annealed samples, which can be attributed to recrystallization reducing work hardening effects. All described features are expected according to the reference data of highly deformed Cu (from Ref. [13]). Nevertheless, while the strengths of the deposits are slightly higher, the elongation of the cold sprayed and annealed sample at 430 °C reaches only 76% of that observed in the cold rolled and annealed reference Cu bulk material after annealing. The improvement of the fracture strain (ε_f) by annealing can be seen as major improvement, confirming ductile deformation at acceptable strength in comparison to the as-sprayed material.

3.3.2. Microhardness

Table 2 also provides data on microhardness. In absence of sample porosity, the microhardness provides information on overall stain hardening effects. Such analyses are needed, since respective tensile test data on strength and strain hardening of as-sprayed deposit might be influenced by non-bonded interfaces acting as crack nuclei. As a consequence of the high degree of particle deformation and respective strain hardening, the as-sprayed deposit shows a high hardness of about 153 $HV_{0.3}$, which is even higher than that of cold rolled to 70% thickness reduction Cu bulk material (125 $HV_{0.3}$) [25]. However, it is worth noting that the hardness of the as-sprayed sample is comparable to that of deposits sprayed by using He as process gas (150 $HV_{0.3}$) [25]. The pronounced decrease in microhardness after annealing is attributed to the reduction of the ultrahigh dislocation densities. Increasing temperature leads to a decrease of microhardness, and thus results in an increase in ductility. The sample annealed at 430 °C still shows higher microhardness (about 68 $HV_{0.3}$) than the annealed bulk copper material (49 $HV_{0.3}$). This difference may be explained by the occurrence of persistent dislocation loops, which were formed by

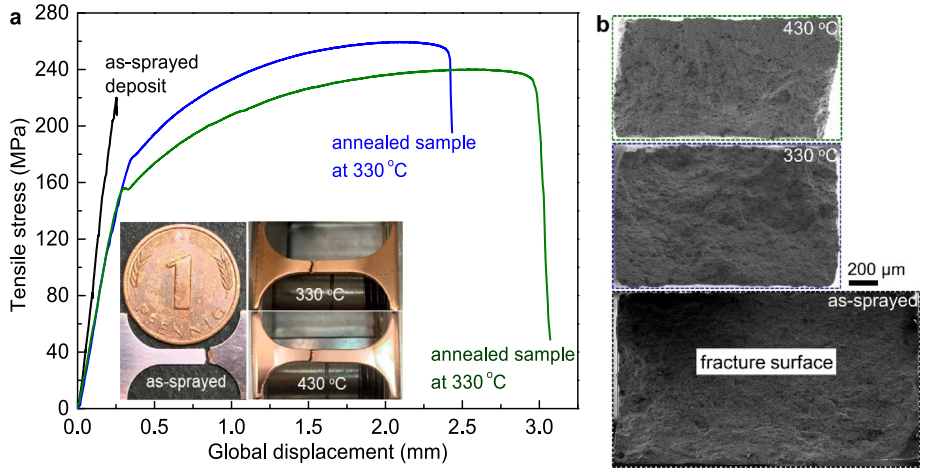

Fig. 8. (a) Stress vs. global displacement obtained by ex-situ tensile testing of notch-free samples. The black, blue and green curves represent the as-sprayed and annealed deposits heated at 330 and 430 °C, respectively. The inset in Fig. a show the macrographs images of fractured samples. (b) Areas of the fracture surfaces used to estimate the fracture strain. (For interpretation of the references to color in this figure legend, the reader is referred to the web version of this article.)

Table 2
Tensile properties and microhardness of the as-sprayed and annealed samples. Mean tensile values are obtained from two measurements for each state. Literature data on highly deformed bulk material are given for comparison.

Samples	UTS (MPa)	Elongation at fracture (%)	Fracture strain (ε_f)	Microhardness ($HV_{0.3}$)
As-sprayed deposit	220	0.4	0.05	153
Annealed deposit at T = 330 °C	259	29	0.49	80
Annealed deposit at T = 430 °C	241	38	0.62	68
Micro-flat sample Cu, cold rolled to 70% [13,25]	385	3	–	125
Micro-flat sample Cu, cold rolled and annealed at 350 °C [13,23]	230	50	–	49

the condensation of point defects obtained by high strain rate deformation [25].

3.4. Microscopic features of crack propagation during in-situ tensile deformation

3.4.1. As-sprayed state

The high-energy impact of solid particles causes microstructures with elongated, highly work hardened grains in direct neighborhood to non-bonded areas and interfaces (compare Fig. 5a-c). The combination of these features with low ductility and existing crack nuclei could facilitate fracture. In order to investigate the role of pre-existing cracks and possible growth mechanisms in direct correlation to the deformed microstructures of the as-sprayed deposit, a pre-notch is introduced at one edge of the in-situ tensile samples (see Fig. 2e). By this, statistically determined growth of the largest flaw somewhere in the sample can be avoided, allowing to observe the development of damages near the notch tip with the high resolution of the SEM. Since samples in the as sprayed state fail before showing plastic deformation (compare Fig. 8), respective force–displacement curves of the in-situ experiments of this condition are not given here. In the microscopical analyses, the initial microstructure (XY plane) before loading is shown here for comparison (Fig. 9a), denoted as stage I_0. The loading is then interrupted during tensile testing in order to take the SEM micrographs at different deformation stages I_1 and I_2, which correspond to a displacement of 0.11 mm and 0.18 mm in Fig. 9b-c, respectively. The final fractured status I_3 is presented in Fig. 9d.

The observation of the fracture process during the in-situ loading and monitoring confirms the brittle behavior of the as-sprayed sample. As compared to stage I_0, no visible deformation of the microstructure can be observed during the loading stages I_1 and I_2 (as circled in Fig. 9a'-c'). At a global displacement of 0.24 mm, here denoted as stage I_3 (Fig. 9d), sudden fracture occurs due to the failure of non-bonded interfaces in the vicinity of the critical crack (i) growth. In addition, secondary crack paths (denoted ii and iii in Fig. 9d') along the particle–particle interfaces near to critical crack (i) are activated. This means that, after a certain load, the critical crack, accompanied by subcritical cracks, initiates from the notch and by growth and bridging into next non-bonded interfaces and leads to failure. Thus, crack growth just occurs along the particle–particle interfaces and joins the already individually grown internal cracks. As compared to the microstructures at lower strain (Fig. 9a'-c'), the local microstructure (Fig. 9d'') near to the critical crack (i) shows no obvious deformation. Further information concerning the fracture behaviors is given by the microstructural details inside the two black rectangles in Fig. 9d. Fig. 9eand f show details of secondary, under-critical crack nuclei development in the surrounding of the main crack, indicating local crack growth and widening already before the stress relief by growth of the main crack. Crack widening to a certain extend might be attributed to plastic deformation inside the deformed particle splats. An example for slip bands close the edge of the main crack is given in Fig. 9f'.

By the high magnification analyses of the deformed and the fractured regimes (Fig. 9e-f), the following conclusions can be drawn for the failure mechanisms of the as-sprayed sample: i) Non-bonded inter-particle boundaries act as pre-existing cracks that could propagate; ii) Many potential cracks are present that are subcritical at local loads given in the vicinity of the first over critical crack; iii) Crack growth occurs by high stress concentrations bridging to next non-bonded interfaces, thus connecting pre-existing defects; iv) Plastic deformation is nevertheless observable in the splat interior. For example, microscopic details reveal slip band formation in the deformed grains (blue arrow in Fig. 9f'); v) The bonded interfaces (green arrows in Fig. 9e) next to the non-bonded ones (black arrow in Fig. 9e) show a ductile behavior. It is attributed to the local dynamic recrystallization during impact.

The non-bonded internal interfaces can act as potential crack nucleation sites, already at quite low elongation at fracture (see Table 2). This is associated with multiple cracks existing in the as-deposited microstructure, see Fig. 9e and f''. Therefore, once an overcritical main crack dominates, it connects to other existing micro-cracks of non-bonded interfaces. All together that leads to catastrophic failure of the material.

3.4.2. Annealed states

Understanding the limited ductility of cold sprayed deposit requires to deal with a number of issues as: i) The amount of non-bonded interfaces that exist after cold spraying; ii) Material properties in the surrounding of bonded and non-bonded

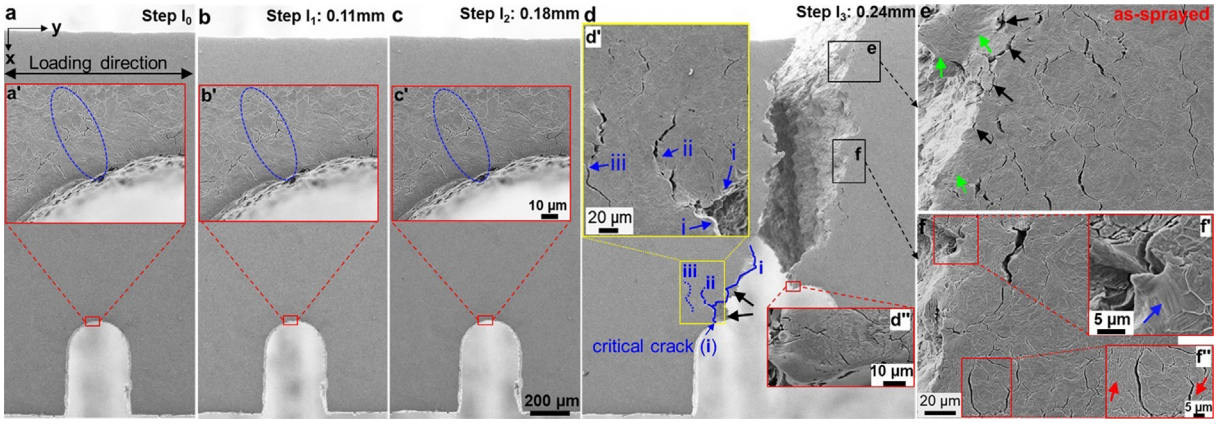

Fig. 9. Microstructural development (SEM images) during in-situ tensile testing of the as-sprayed sample at different displacements. SEM images at the loading stages I_0-I_3 are provided in Fig. a-d. The inserts represent the microstructures at high-magnification as marked by the rectangles. Fig. d'' shows the microstructure in the vicinity of the critical crack (i), in turn indicating the corresponding crack initiation site as marked by blue dashed ellipse in Fig. a'-c'. The black arrows in d indicate the fractured surfaces below the XY plane. Fig. e and f are taken from the areas marked by the black rectangles in Fig. d. The black and green arrows in Fig. e show the brittle non-bonded interfaces and the more ductile well bonded interfaces in their direct surrounding, respectively. The details (Fig. f' and f'') are taken from the regions inside the red boxes in Fig. f. The blue and red arrows in (f') and (f'') indicate the slip bands and the severely localized deformation areas, respectively. (For interpretation of the references to color in this figure legend, the reader is referred to the web version of this article.)

interfaces in the highly deformed and work hardened state; iii) The load transfer in the vicinity of cracks (non-bonded interfaces) or defects to less deformed areas that can restrict crack propagation.

Effects associated with atomic diffusion during annealing can reduce the above-mentioned origins of crack growth. Also for annealed samples, a pre-notch is introduced to define areas for investigating the crack path using the in-situ SEM analysis during tensile testing. As compared to the as-sprayed state, the sample annealed at 330 °C (denoted here as stages II) shows a UTS and substantially larger elongation to failure (see Table 2 and Fig. 8). Increasing the annealing temperature to 430 °C (denoted here as stages III) leads to slightly reduced UTS and in turn in a larger elongation to failure than obtained after annealing at 330 °C. As before, also for the annealed samples, interrupted loadings stages (see Fig. 10) are applied to observe the local fracture behavior during tensile deformation. The planar views of pre-notched samples after fracture corresponding to stages II7 and III7 are shown by the inset in Fig. 10. In contrast to the α_{II} for the sample annealed at 330 °C, a larger bending angle of α_{III} for the sample annealed at 430 °C is observed, which can be attributed to a rather higher global displacement as seen by the inset in Fig. 10.

Possible crack propagation depends on the largest flaw dimensions as nuclei, in the present case thus the size of the existing non-bonded interfaces, as well as on the stress levels that can be induced over distance to allow coalescing to the next flaws. Fig. 11 and Fig. 12 compare the crack propagation behaviors at different notch elongation of the samples annealed at 330 °C and 430 °C, respectively. The notch elongation, $\varepsilon = (n\text{-}n_0)/n_0 \times 100$, has been calculated from the initial notch width (n_0) and notch width (n) at corresponding loading stages. For the sample annealed at 330 °C, at stage II_1, the notch width shows an increase of about 54%, as compared to stage II_0, prior to loading (Fig. 11). At this stage, most severally deformed areas (red dashed rectangle) are observed near the center of the notch region. After deformation, grain elongation (black circle), slip band formation (black arrows), micro-crack nucleation (yellow rectangle) and micro-void enlargement (yellow arrow) are already observed. After an increasing the notch elongation to 71% (stage II_2), two cracks start to form, later in stage II_3 identified as the main crack (i) and a subcritical crack (ii). From stage II_3 to stage II_5, the main crack grows. The coalescence with newly formed micro-cracks in the vicinity of the crack tip, means areas of high stress concentration, leads to the formation of a macroscopic crack (i). The growth of the first subcritical crack (ii) appears to be terminated after stage II_3, obviously due to the drop in local stresses after growth of the dominating one (i). During propagation of the main crack (i), many local micro-cracks (blue arrows in red inset at stage II_4) are observed around the main crack tip. The largest crack among them (yellow arrow in red inset at stage II_4), which is ahead of the main crack tip, is coalescing with the main crack tip. The others far away from the main crack tip (blue arrows in red inset at stages II_4 and II_5), are trapped in their initial growth state by the local stress release. Subsequently, at stage II_5, the main crack bridges to the largest micro-crack in the volume ahead (yellow arrow in red inset at stage II_4), thus driving the crack propagation. Since the defects are randomly distributed in the microstructure, the main crack reorients to join with local micro-cracks. During the main crack propagation, both transgranular (blue inset at stage II_4) and intergranular fracture (blue inset at stage II_5) is observed. When the sample was loaded to stage II_6, the notch elongation reaches about 125%. At this stage, the area ahead of the main crack tip is heavily deformed. By coalescence with local volume cracks, a crack bifurcation upon loading occurs. Summarizing up to sample failure at a notch elongation of 177% (stage II_7), diversions on the zigzag fracture path lead to a highly structured fracture topography. This is similarly observed for the whole sample thickness as seen here for stage II_6 and stage II_7, showing a view of the opened crack. However, it cannot be judged to which extent large flows inside the volume influence the observed crack propagation at the surface.

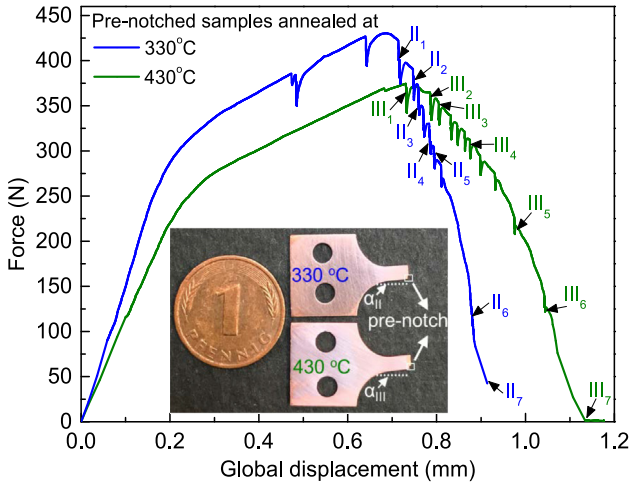

Fig. 10. Force vs. displacement curves of in-situ SEM tensile testing. The blue and green curves represent the pre-notched samples annealed at 330 and 430 °C, respectively. The load drop denotes the stress relaxation that occurred when the test was interrupted for observing the deformed microstructure. The inset shows photographic images corresponding to the final stages II_7 and III_7, i.e. the planar views of pre-notched samples after fracture. (For interpretation of the references to color in this figure legend, the reader is referred to the web version of this article.)

In comparison to the crack propagation of the sample annealed at 330 °C, the deformation and failure behavior is different for the sample that was annealed at 430 °C (Fig. 12). The initial microstructure, before loading, is denoted as stage III_0, and shows quite small pre-existing voids as observed at higher magnification (see blue arrows in the insert and Fig. 7e-f). Similar to stage II_1 (Fig. 11), the first micro-crack (i) forms along the slip bands (see black arrows) and during propagation spreads towards a pre-existing and enlarging pore directly (see blue arrow) at stage III_1 (Fig. 11b), due to the localized stress in the notch region. At this loading stage, no other micro-cracks are visible. With a continuous plastic deformation to stage III_3 (corresponding to a notch elongation of 119%), the primary crack (i) coalesces with the grown void developed early (see the insert at stage III_1). In addition, a secondary crack, referred to as (ii), is generated (see insert). After a slight increase of notch elongation to 143% in stage III_4, the secondary crack (ii) grows and propagates as macrocrack at about the middle of the notch edge, here the local stress is the highest. Local deviations in growth direction are supposed to be driven by the local deformation and occurring micro-cracks in the vicinity of the crack tip (red arrows in insert at stage III_4). During the main crack propagation as illustrated by stages of III_5 and III_6, in contrast to the sample annealed 330 °C, no serious damage or secondary cracks can be found nearby or ahead of the main crack tip. Therefore, at these later stages, the crack morphology exhibits less fluctuations. This behavior of crack propagation can be related to better particle–particle interface bonding and lower amounts of potential micro-cracks being present in the area of high stress concentration in front of the crack tip. The final failure (stage III_7, in Fig. 12) occurs at a notch elongation of 253%. As visible from the force–displacement curves and here by the notch elongation, final failure occurs at significantly higher fracture strain than for the sample being annealed at 330 °C. Comparing the deformation and failure behavior after the two annealing conditions, it can be concluded that a higher annealing temperature is more favorable for enhancing the material ductility and the resistance against fracture due to reduction of non-bonded interfaces, spheroidization of voids and improvements in internal interface fracture toughness.

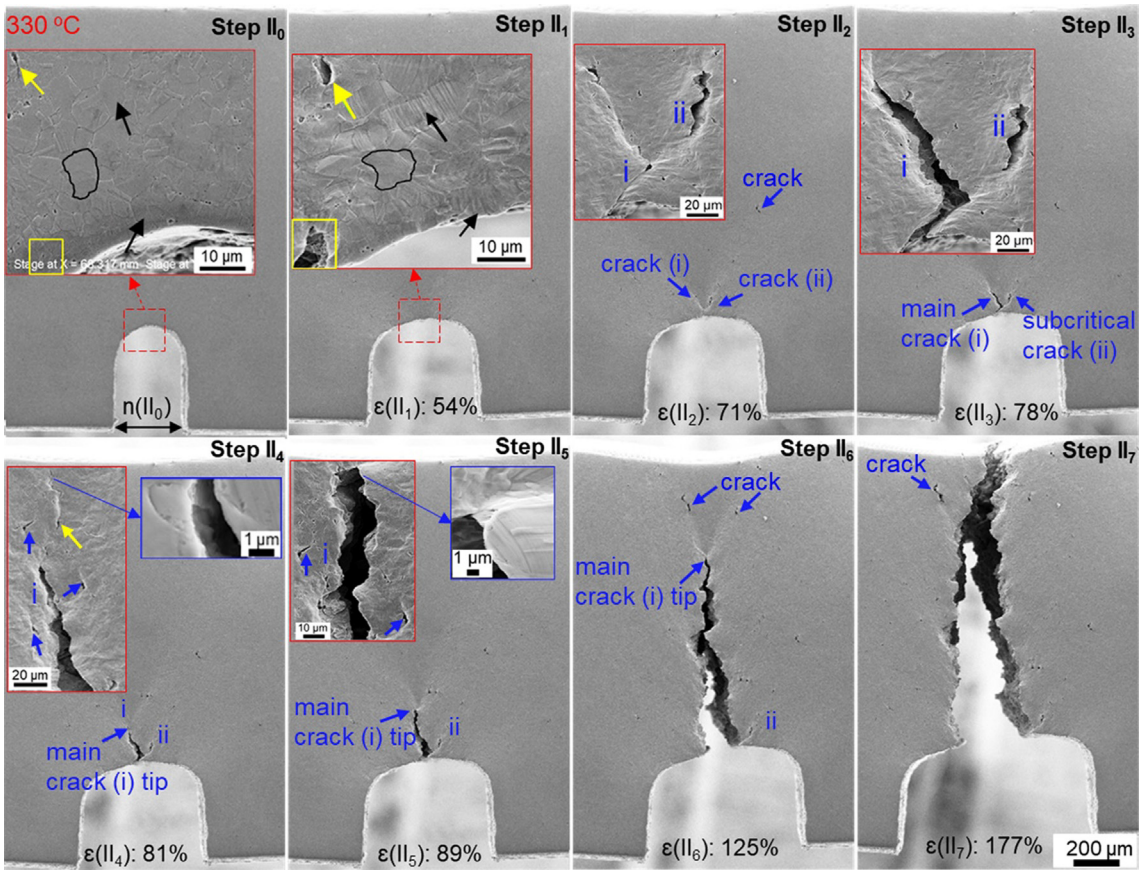

Fig. 11. Microstructural development during in-situ tensile testing of a pre-notched sample annealed at 330 °C. SEM images at lower magnification correspond to the different loading stages given with the blue curve in Fig. 10. The values of notch elongation, ε (II_1-II_7), are indicated in the corresponding notch regions. The red inserts of SEM images (from stage II_0 to stage II_5) at higher magnification show more details on the deformed areas. The blue insets of SEM images at stage II_4 and II_5 show the transgranular fracture and intergranular fracture, respectively. (For interpretation of the references to color in this figure legend, the reader is referred to the web version of this article.)

3.4.3. Deformation and failure morphologies

In order to gain additional information on the fracture mechanisms, detailed fractographic analyses by SEM of notch-free tensile samples (refer to Fig. 8b) were conducted. Fig. 13 summarizes the typical fracture morphologies for the three different conditions. Fig. 13a-b show typical fracture surfaces of the as-sprayed state with multiple cracks at interparticle boundaries (arrow of i, in Fig. 13a), which correlates well with the observations shown in Fig. 9f'. However, already in the as-sprayed state, most of the fracture features correspond to metallurgically bonded splats, as given in Fig. 13b by the example of a different, dimple-like plastic deformation pattern (arrows of ii and iii). As shown in Fig. 13a, even transgranular failure or cleavage (arrow v) is observed. Only about 40–50% of the failure occurs as inter-splat failure (arrow vi) at non-bonded internal interfaces (arrow vii), which is in good agreement to the results on deposit microstructures (Fig. 5) and microstructural development during in-situ tensile testing (Fig. 9). The areas of metallurgical fracture show different modes, ranging from ductile dimple failure under plastic deformation to faceted cleavage of highly work-hardened areas. This variety of fracture morphologies correspond to the different microstructural features as obtained by cold spraying. With respect to local appearance, however also effective local stresses, stress gradients in the vicinity of micro- or macro-cracks, as well as local differences in strain hardening can play a role. All these effects also govern possible deviations in crack growth direction and partially bridging through splat interiors (Fig. 9e, f').

Fig. 13c-d show fracture surfaces of the deposits after annealing of 330 °C. As given in Fig. 13a, most of the fracture surface is covered with heterogenous dimple colonies (arrows of ii). The different dimple sizes (arrows of ix and x) can be attributed to microstructural inhomogeneities, here probably given by grain sizes and local differences in deformability with some areas yet not fully recrystallized (partially work hardened areas). This is in good agreement with the obtained deposit hardness (see Table 2) and the microstructure development during in-situ tensile testing. Only very few amounts of the fracture surface show flat features (arrow viii) that correspond to pre-existing crack sites of non-bonded interface. In the sample annealed at 330 °C, the few flat surfaces being present after fracture demonstrate that not all non-bonded interfaces (arrows i) are sintered by surface diffusion, which might guide the local crack deviation shown in Fig. 11 for in-situ analysis. The sample annealed at 430 °C (Fig. 13e-f) presents a fracture surface that is nearly completely covered by rather uniform dimples. Former splat shapes or interparticle boundaries are not identified anymore. The dimple sizes show a wider range, correlating with the coarser grains, than those of the sample annealed at 330 °C (Fig. 6). Moreover, the dimple features indicate that the fracture of the sample annealed at 430 °C is driven by void nucleation, growth and coalescence, as revealed by significant dimple enlargements (arrow ix) on the fracture surface.

4. Discussion

4.1. Deposit property prediction

The relations between the deposit cohesive strength σ_c, the particle velocity v_p, the critical velocity v_{cr}, as well as the deposit

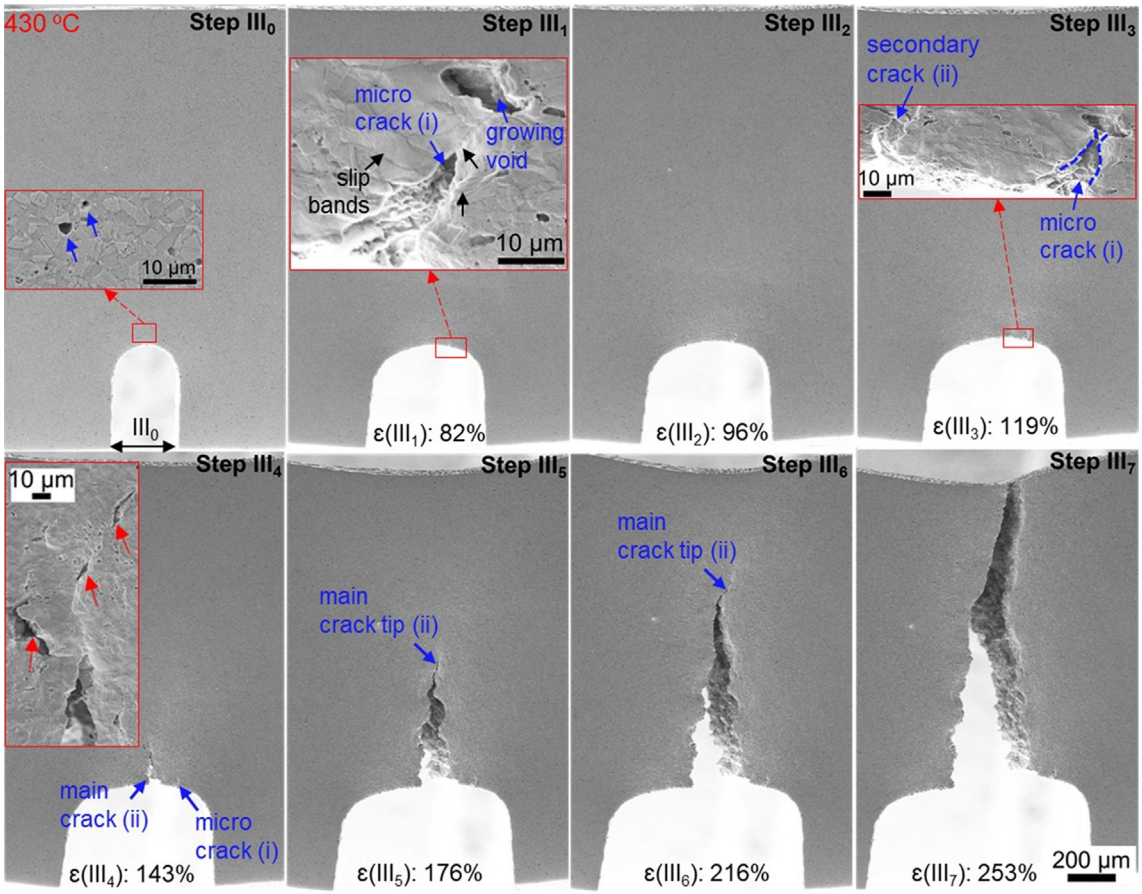

Fig. 12. Microstructural development during in-situ tensile testing of the pre-notched sample annealed at 430 °C. SEM images correspond to the different loading stages given with the green curve in Fig. 10. The values of notch elongation, ε (III_1-III_7), are noted in the corresponding notched regions. Inserted SEM micrographs at higher magnification show details on the deformation and failure mechanisms. (For interpretation of the references to color in this figure legend, the reader is referred to the web version of this article.)

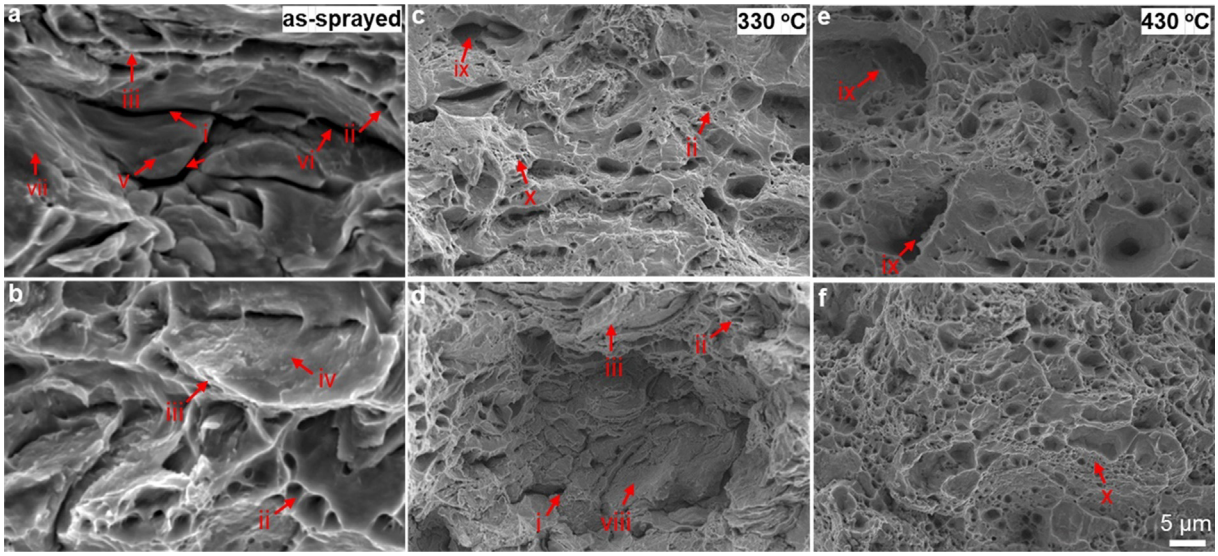

Fig. 13. Fracture surface of the as-sprayed (a-b) and two annealing states at 330 (c-d) and 430 °C (e-f). The arrows indicate features of i: crack growth at non-bonded interfaces, ii: dimples, iii: rupture of well-bonded areas showing low strain, iv: bonded area with high deformation, v: brittle transparticle fracture, vi: crack opening sites at inter-splats boundaries, vii: non-bonded interfaces, viii: flat interface by inter-splat failure, ix: dimple enlargement, and x: fine dimple fracture.

quality parameter η were described in detail in Refs. [11] and [17]. Based on the experimental data of σ_c and v_p in Ref. [11], Assadi et al. [17] demonstrated that the variation of the cohesive strength with v_p/v_{cr} is identical for all powder sizes. For comparing the present results with literature, Fig. 14 shows respective correlations between σ_c and η together with the data from reference [17]. In

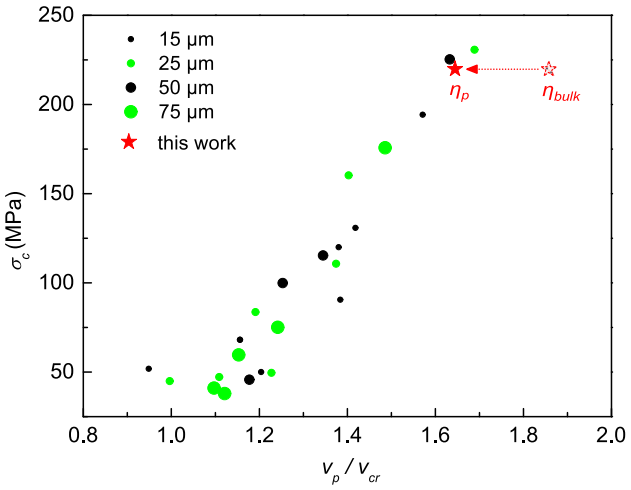

Fig. 14. Tensile strength of as-sprayed Cu deposits as a function of the ratio η between the particle impact velocity and the critical velocity. Data for different powder sizes (black and green dots) refer to critical velocities according to Ref. [17] and deposit strengths from Ref. [11]. Data of the present work refer to calculating critical velocities alternatively on the basis of particle strength (η_p) or bulk strength (η_{bulk}). (For interpretation of the references to color in this figure legend, the reader is referred to the web version of this article.)

the present case, critical velocities and thus the v_p/v_{cr} ratios were calculated by alternatively using the bulk Cu material data and individually determined primary powder strengths. The comparison shows that the observed strength σ_c of the as-sprayed Cu deposits (here 220 MPa, see Table 2) only follows the general trend when powder strengths are used as input data. This underlines the necessity to use experimentally determined powder properties for calculating critical velocities for reliable prediction of deposit performance. In addition, the agreement demonstrates that deviations from spherical shape of the used powder feedstock at least for present case only has minor influence on the deformation and thus v_{cr}. Also, differences with respect to particle acceleration by higher drag forces of more angular powder and the use of a different spray systems seem to be tuned by respective calibration factors in KSS-software. In summary, the so far established dimensionless parameter η -if properly based on the initial powder strength- allows for a good prediction of deposit quality regardless of spraying system and morphology of sprayed powder.

4.2. Ductility and tensile strength

According to literature, OFHC copper by work hardening (thickness reduction of 97.5%) can reach an UTS of about 427 MPa [27]. Cold rolling to high thickness reduction results in a saturation regime due to dynamic recrystallization during cold working [27,28]. Assuming maximum work hardening of the as-sprayed deposits, the determined strength of 220 MPa corresponds to about 52% of metallurgically bonded areas that carry possible loads, in rather well agreement to the observed microstructures (Fig. 5a-c). The real situation however is more complicated, since also local fracture toughness and stress concentration induced by the non-bonded interfaces as crack nuclei have to be taken into account. Thus, the real amount of metallurgically bonded interfaces can be higher than estimated using such simple assumptions. In addition, the combination of pre-existing crack-nuclei and highly work hardened/low ductility surroundings results in overall low strain to failure of as-sprayed deposits.

To tackle these shortcomings, the recovery and recrystallization during annealing of the deposits can improve strength and ductility [12,13,19,20,25], see Table 2. On the one hand, the surface diffusion along non-bonded interfaces during annealing can reduce or even close such pre-existing crack nuclei. On the other hand, recovery and recrystallization naturally improve the ductility and fracture toughness. Fig. 15a summarizes the present results on the elongation to failure together with data from literature for different as-sprayed and annealed deposits, as well as for rolled and annealed bulk Cu material. In the as-sprayed state, the sample processed with N_2 as process gas [13] shows an elongation at fracture smaller than <1%, which is lower than that of deposit cold sprayed with He as process gas (2%, [13]) and the bulk material cold rolled to 70% thickness reduction (3%, [13]). After subsequent annealing at temperatures of maximum 600 °C, the elongation at fracture of the samples processed with He and N_2 can be improved to a strain to failure of maximum 8% [13] and 24% [13], respectively, which are still lower than the elongation of the soft annealed bulk Cu (50%, [13]). This means that, after annealing, microstructural defects still exist, which limit further deformation. This also applies to the N_2 processed sample annealed at 330 °C of the present work showing only 29% elongation to failure, which is much lower than that of bulk Cu material [13]. This is due to the few amounts of non-bonded areas that are still present after low-temperature annealing, as demonstrated by the analyses of fracture surfaces presented in Fig. 13d.

By increasing the annealing temperature to 430 °C, the sites for crack initiation are drastically reduced, thus allowing for a higher degree of plastic deformation and a strain to failure of about 38%. The significantly lower amount of defects was confirmed by observing the fracture surface morphologies shown in Fig. 13e-f, which predominantly reveal ductile failure and uniformly distributed dimples. By diffusion at this higher temperature, the number of all sorts of internal defects left in the as-sprayed state can be reduced and remaining voids are spheroidized, causing the observed improvement of ductility.

Fig. 15b compares the ultimate tensile strengths of as-sprayed and annealed samples from the present study with those reported in literature. In this comparison, only deposits processed with He as process gas reveal a similar performance and decrease of strength with increasing annealing temperature as cold rolled bulk material [13]. The rather similar behavior is attributed to the high degree of work hardening attained by cold spraying with He. Considering the microhardness as a global measure for work hardening by cold working, the amount of deformation, revealing the average dislocation density, in the as-sprayed sample by using He gas is higher than that of bulk Cu cold rolled to 70% thickness reduction [13], which is in good agreement to the measured strength. In comparison to the He processed samples or cold rolled bulk Cu samples deposited using N_2 as process gas show lower strengths in initial as-deposited state, which then increases with annealing temperatures. For spray conditions with higher process gas temperature used in literature [12], at an annealing temperature of about 400 °C, a similar strength of about 270 MPa is achieved as for the deposit sprayed with He as process gas. This is due to the fact that the surface diffusion at low temperature annealing can already reduce the present low amounts and sizes of non-bonded interfaces to a decent extent, i.e. not being critical for crack nucleation. As a result, the strength increases with annealing temperature. On the corresponding fracture surfaces (Fig. 13c), dimple-like patterns observed for the low annealing temperature of 330 °C indicate ductile failure. However, such lower annealing temperatures might not be sufficient for activating recrystallization within areas of low dislocation densities [13]. Thus, respective deposits show higher hardness and UTS than fully recrystallized ones [25]. Only the coatings sprayed with significantly lower gas temperature, need higher annealing temperatures for reaching bulk-like properties [13]. This may be attributed to the too high amounts and too large sizes of non-well bonded interfaces. For the deposits sprayed

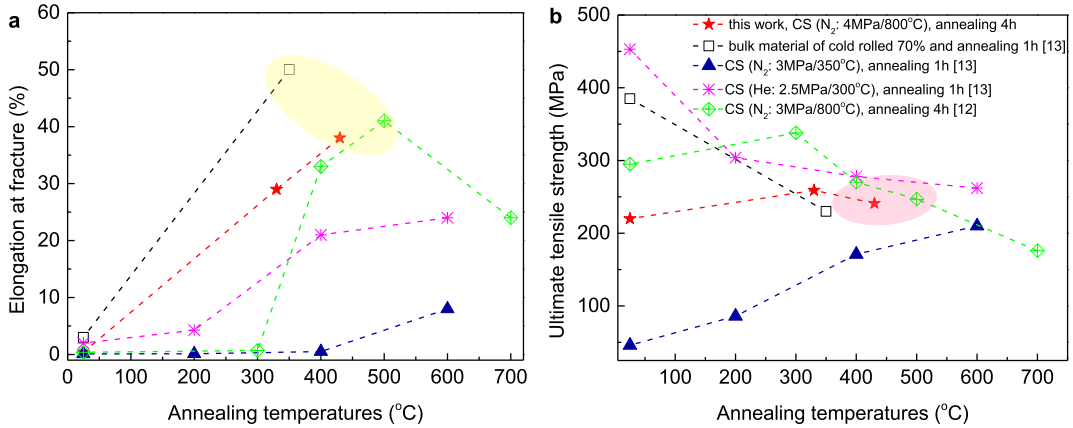

Fig. 15. Elongation to failure (a) and ultimate tensile strength (b) of Cu deposits for the as-sprayed state and various annealing conditions using different temperatures. The red curve denotes the data of the present work. For comparison, data for cold rolled and annealed bulk Cu are included in the graph, as presented by the black curve. (For interpretation of the references to color in this figure legend, the reader is referred to the web version of this article.)

at 800 °C, annealing temperatures greater than 400 °C result in a decrease of strength (present work and ref. [12]). This could be attributed to grain growth, which will lead to a further decrease in strength and hardness. Even at high annealing temperatures, defects could be still present in the deposits. These defects are non-bonded interfaces as crack nuclei or free volume from micro-cracks, accumulated to micro-voids. However, work hardening by high dislocations densities will be completely eliminated by recrystallization. In comparison to bulk material, a higher hardness of CS-deposits annealed at higher temperatures (compare Table 2) can be attributed to the presence of persistent dislocation loops [26].

With respect to possible applications, it is of high interest that the deposit sprayed with N_2 gas, after annealing at 430 °C, shows a similar performance concerning the elongation to failure and the ultimate tensile strength, as highly deformed and annealed bulk Cu, as illustrated by the colored areas in Fig. 15. It means that cold spraying of Cu with N_2 gas, combined with annealing at a suitable temperature between 400 and 500 °C, can be considered as an economical alternative to the costly utilization of He as process gas.

4.3. Influences on deposit failure

The results on the different failure modes of as cold sprayed and of annealed deposits demonstrate the influence of the highly heterogenous microstructures and defects in as-deposited state and respective effects by reducing amounts and sizes of defects by annealing. The observations in Sections 3.2 and 3.4 allow to summarize mechanisms of crack propagation for various microstructures that are attained under different annealing conditions as proposed by Fig. 16.

In the as-sprayed condition, deposit failure is associated with crack growth and the present defects. Crack growth is supported by (1) the amounts and sizes of pre-existing cracks as non-bonded internal interfaces (i_1) between spray splats (i_2), and (2) the low ductility and fracture toughness of the work hardened, bonded material (i_3) in the surrounding of such crack nuclei. Both, the size of pre-existing cracks, and the limited ductility determine the stress concentration in the vicinity of the crack tip (i_4) and thus possible crack growth paths (i_5).

Particularly, the in-situ microstructural observation during tensile testing provides lively information on the mechanisms of crack development and growth. The most important information by these analyses concerns the formation of multiple crack nuclei at almost all non-bonded interfaces loaded to sufficiently high stresses, demonstrating the rather rigid, mainly elastic behavior of spray splats in the as-deposited state. This reveals the complex interplay between non-bonded interfaces as crack nuclei and the influence of work hardening and reduced fracture toughness in the vicinity of internal interfaces for restricting further plastic deformation of splats. Plastic deformation only spreads through areas that have been subjected to dynamic recrystallization at particle–particle interfaces (i_6 and green arrows in Fig. 9e) [29] or if *trans*-splat fracture involves the less strain hardened particle interior (i_7). In consequence, failure of as-sprayed deposits is associated with (a) separation of non-bonded interfaces by crack growth, (b) rupture of work hardened areas (i_8), (c) ductile deformation and respective dimple failure (i_9) and (d) crack path diversion to transparticle failure (i_7). Only the latter both (c) and (d) result in ductile deformation pattern.

Annealing reduces the sizes or even eliminates present defects. Pre-existing cracks/non-bonded interface are reduced by surface diffusion and sintering [13]. The in-situ testing of the sample annealed at the lower temperature of 330 °C demonstrates that, despite a globally rather ductile behavior, locally none perfectly closed crack-nuclei at non-bonded interfaces (ii_2) initiate sample fracture, as schematically visualized by occurrence of secondary cracks (ii_5 and ii_7 in Fig. 16) in region of sufficiently high stresses.

Recrystallization increases the ductility and toughness by reduced dislocations densities. All that leads to microstructure homogenization, especially for the sample annealed at 430 °C (iii_1 in contrast to ii_1), in an ideal case similar to that of annealed highly work hardened bulk material, as schematically shown in Fig. 16. Note that the non-uniform dislocation densities in cold sprayed deposits might need higher annealing temperatures than highly deformed bulk material for activating recrystallization also in areas of less deformed particle cores.

As mentioned in Section 3.2.2, all non-bonded interfaces are apparently eliminated in the sample annealed at 430 °C, which has also been evidenced through the analysis of fracture surfaces (Fig. 13e-f). Though some larger voids resulting from the growth of the free volume of non-bonded interfaces tend to appear (see iii_2 and Fig. 7e-f), respective extensions are smaller than that of non-bonded interfaces (Fig. 7) and they are further apart, so there is more room for void growth before crack coalescence. Their spherical shape results in lower stress concentration in their vicinity, suggesting a higher tolerance for more damage before failure than the deposit annealed at 330 °C. As a result, the deposit annealed at 430 °C reaches a higher ductility.

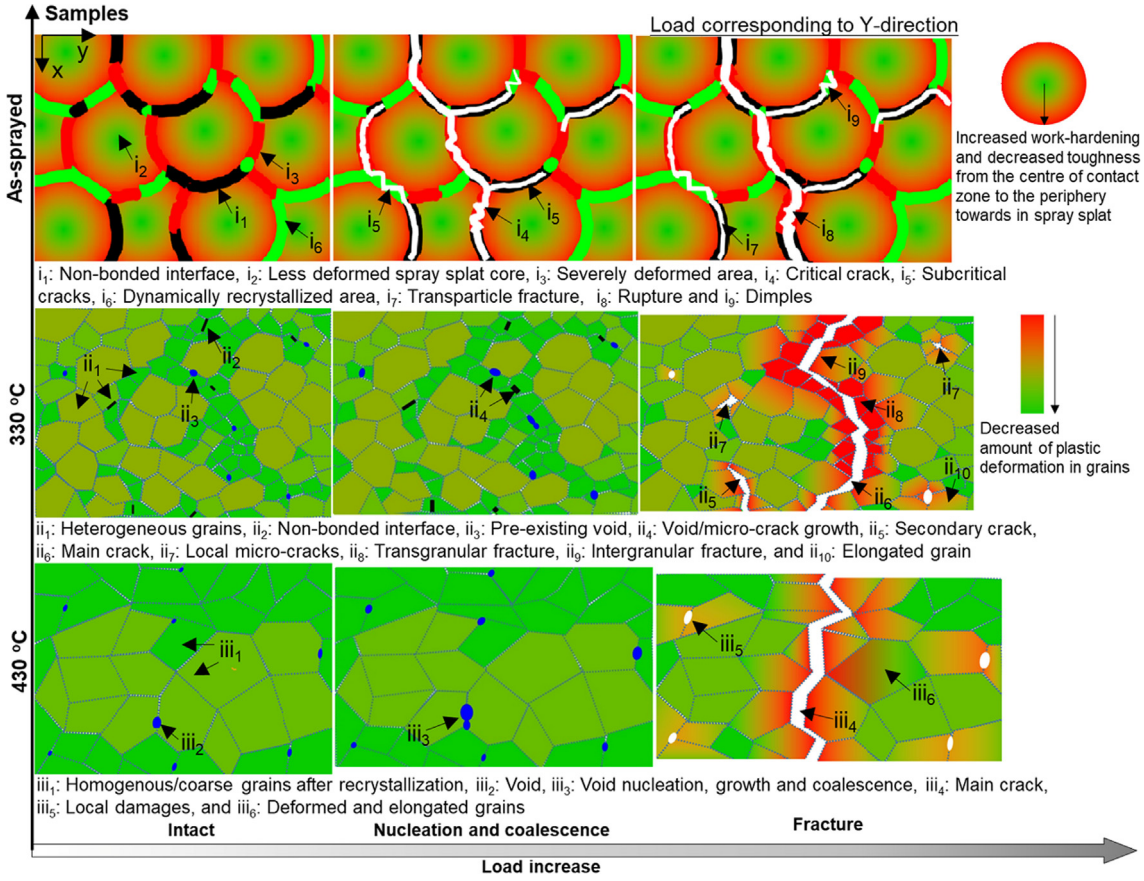

Fig. 16. Schematic for the crack development in the different microstructures of CS Cu deposits attained in the as-sprayed deposit and after annealing at 330 and 430 °C (top view, XY plane). It is assumed that loads are applied in Y-direction. The inserted arrows indicate the respective fracture mechanisms for the different annealing states. The color code in the schematic indicates the amount of plastic deformation for the spraying splat and the recrystallized grains.

Additional information on the development of the different defects with annealing and respective consequences on deposit failure can be revealed by notch elongation and main crack length analysis. The analyses of elongation, i.e. the differences between the current and the initial notch widths, can provide more accurate information on local deformation states than the global displacement, which involves the deformation of the whole tensile set-up. Respective data on main crack length are plotted in Fig. 17 versus the observed notch elongation taken from Fig. 11 and Fig. 12, here serving as measure for strain. The analyses of the crack growth behavior show that annealing at the lower temperature of 330 °C (blue curve) leads to crack propagation starting at lower strain as compared to that of the sample annealed at 430 °C (green curve). Moreover, the slopes indicate a slightly faster crack growth rate for the lower annealing temperature.

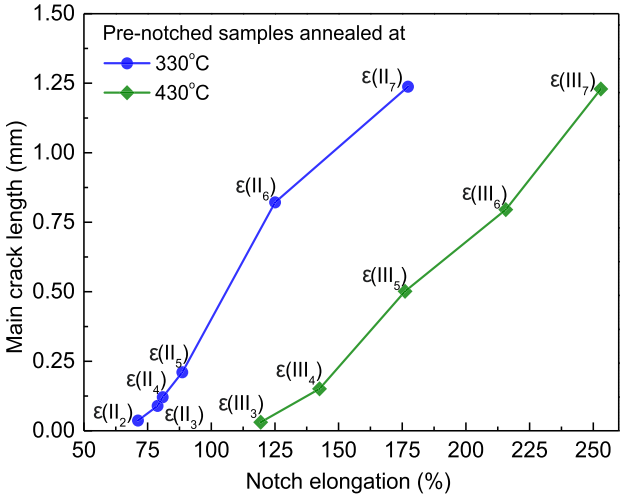

Fig. 17. Main crack length vs. notch elongation as observed in-situ tensile tests of the pre-notched samples. The individual crack lengths and notch elongations are obtained from Figs. 11 and 12.

5. Summary and conclusions

For cold sprayed and respectively annealed copper deposited, the present study correlates macroscopic properties with the associated mechanism of crack growth. The first prerequisite to obtain high deposit quality by cold spraying is to ensure a high quality parameter η. At second instance, deposit annealing can be tuned for adjusting final properties. The study confirms that the parametric expression of η_p, based on the powder strength and primary process parameters is a suitable tool to predict the deposit properties. The properties obtained in the as sprayed state can be improved by subsequent annealing, resulting in higher fracture strain. For depositing samples under appropriate parameter sets with nitrogen as process gas, an annealing temperature of at 430 °C proved to be sufficient to gain a similar performance as annealed highly work hardened bulk material or annealed samples that have been processed by using much costly helium.

The necessity of annealing was proved by detailed fracture analyses. Failure of the as-sprayed sample is dominated by a rather brittle cleavage-like fracture with mainly inter-splat failure. In

contrast, in the annealed samples a ductile behavior with classical dimples determines final fracture. The ductile behavior is due to spheroidization and reduction of inter-particle defects and recovery and recrystallization of highly work hardened areas. For the selected cold spray conditions within an η range > 1.5, an annealing temperature of 430 °C is sufficient to decrease potential crack initiation sites to acceptable ranges, mainly dealing with possibly remaining micro-voids left over from spheroidized 2D defects as resulting from non-bonded interfaces. In addition, samples annealed at an only slightly lower temperature of 330 °C suffer from fracture by growth of defects, such as remnants from non-bonded interfaces and locally insufficient toughness.

In these investigations, in-situ SEM analysis during tensile testing proved as powerful tool to identify microscopic failure mechanisms by non-bonded interfaces as crack nuclei and limited toughness to allow for crack growth. This allowed to analyze flow formation and the detailed growth study of the finally dominating crack causing fracture. It also confirmed the necessity of reaching defect free deposits to gain bulk like properties.

The findings of this work contribute to the understanding of the relationship between spraying parameter and mechanical properties of deposits and help to associate macroscopic properties with detailed fracture mechanics. It can contribute to developing spraying strategies and post-spraying annealing procedures for reaching mechanical properties similar to those of bulk material and should be also transferrable to other CSAM materials.

Declaration of Competing Interest

The authors declare that they have no known competing financial interests or personal relationships that could have appeared to influence the work reported in this paper.

Acknowledgements

C.J. Huang acknowledges the financial support of Alexander von Humboldt Foundation. A. Simar acknowledges the financial support of European Research Council for a Starting Grant under grant agreement 716678, ALUFIX project. M. Arseenko acknowledges the support of Fonds de la recherche scientifique-FNRS (FRIA grant), Belgium. Y.C. Xie acknowledges the supports of National Natural Science Foundation of China (52001078), Guangdong Basic and Applied Basic Research Foundation (2019B1515120016), and Key-Area Research and Development Program of Guangdong Province (2020B0101330001). W.Y. Li acknowledges the supports of National Natural Science Foundation of China (52061135101). The author acknowledges L.K. Huang at HKU for the aesthetic guidance on the figures, also acknowledges T. Breckwoldt, M. Kollmeier, M. Schulze and C. Schulze at HSU and L. Ryelandt at UCLouvain for substantial support in sample preparation and analysis.

References

[1] E.O. Olakanmi, R.F. Cochrane, K.W. Dalgarno, A review on selective laser sintering/melting (SLS/SLM) of aluminium alloy powders: processing, microstructure, and properties, Prog. Mater. Sci. 74 (2015) 401–477.
[2] D. Herzog, V. Seyda, E. Wycisk, C. Emmelmann, Additive manufacturing of metals, Acta Mater. 117 (2016) 371–392.
[3] D. Bourell, J.P. Kruth, M. Leu, G. Levy, D. Rosen, A.M. Beese, A. Clare, Materials for additive manufacturing, CIRP Ann. Manuf. Technol. 66 (2017) 659–681.
[4] S. Yin, P. Cavaliere, B. Aldwell, R. Jenkins, H.L. Liao, W.Y. Li, R. Lupoi, Cold spray additive manufacturing and repair: Fundamentals and applications, Addit. Manuf. 21 (2018) 628–650.
[5] H.J. Wu, X.L. Xie, M.M. Liu, C. Verdy, Y.C. Zhang, H.L. Liao, S.H. Deng, Stable layer-building strategy to enhance cold-spray-based additive manufacturing, Addit. Manuf. 35 (2020) 101356.
[6] C.M. Sample, V.K. Champagne, A.T. Nardi, D.A. Lados, Factors governing static properties and fatigue, fatigue crack growth, and fracture mechanisms in cold spray alloys and coatings/repairs: a review, Addit. Manuf. 36 (2020) 101371.
[7] T. Schmidt, F. Gärtner, H. Assadi, H. Kreye, Development of a generalized parameter window for cold spray deposition, Acta Mater. 54 (2006) 729–742.
[8] H. Assadi, H. Kreye, F. Gärtner, T. Klassen, Cold spraying- a materials perspective, Acta Mater. 116 (2016) 382–407.
[9] S. Yin, J. Cizek, J. Cupera, M. Hassani, X.T. Luo, R. Jenkins, Y.C. Xie, W.L. Li, R. Lupoi, Formation conditions of vortex-like intermixing interfaces in cold spray, Mater. Des. 200 (2021) 109444.
[10] S. Bagherifard, J. Kondas, S. Monti, J. Cizek, F. Perego, O. Kovarik, F. Lukac, F. Gärtner, M. Guagliano, Tailoring cold spray additive manufacturing of steel 316 L for static and cyclic load-bearing applications, Mater. Des. 203 (2021) 109575.
[11] T. Schmidt, H. Assadi, F. Gärtner, H. Richter, T. Stoltenhoff, H. Kreye, T. Klassen, From particle acceleration to impact and bonding in cold spraying, J. Therm. Spray Technol. 18 (2009) 794–808.
[12] R.Z. Huang, M. Sone, W.H. Ma, H. Fukanuma, The effects of heat treatment on the mechanical properties of cold-sprayed coatings, Surf. Coat. Technol. 261 (2015) 278–288.
[13] F. Gärtner, T. Stoltenhoff, J. Voyer, H. Kreye, S. Riekehr, M. Koçak, Mechanical properties of cold-sprayed and thermally sprayed copper coatings, Surf. Coat. Technol. 200 (2006) 6770–6782.
[14] S. Yin, R. Jenkins, X.C. Yan, R. Lupoi, Microstructure and mechanical anisotropy of additively manufactured cold spray copper deposits, Mater. Sci. Eng. A. 734 (2018) 67–76.
[15] H.J. Wu, C.J. Huang, X.L. Xie, S.W. Liu, T. Wu, T. Niendorf, Y.C. Xie, C.M. Deng, M. Liu, H.L. Liao, S.H. Deng, Influence of spray trajectories on characteristics of cold-sprayed copper deposits, Surf. Coat. Technol. 405 (2021) 126703.
[16] J. Perry, P. Richer, B. Jodoin, E. Matte, Pin fin array heat sinks by cold spray additive manufacturing: economics of powder recycling, J. Therm. Spray Technol. 28 (2019) 144–160.
[17] H. Assadi, T. Schmidt, H. Richter, J.O. Kliemann, K. Binder, F. Gärtner, T. Klassen, H. Kreye, On parameter selection in cold spraying, J. Therm. Spray Technol. 20 (2011) 1161–1176.
[18] Impact Innovations GmbH Germany, https://impact-innovations.com/werkstoffe/cu/ (accessed on 2021.04.25).
[19] B. Yu, J. Tam, W. Li, H.J. Cho, J.G. Legoux, D. Poirier, J.D. Giallonardo, U. Erb, Microstructural and bulk properties evolution of cold-sprayed copper coatings after low temperature annealing, Materialia 7 (2019) 100356.
[20] S. Singh, S. Chaudhary, H. Singh, Effect of electroplated interlayers on properties of cold-sprayed copper coatings on SS316L steel, Surf. Coat. Technol. 375 (2019) 54–65.
[21] H. Assadi, I. Irkhin, H. Gutzmann, F. Gärtner, M. Schulze, M.V. Vidaller, T. Klassen, Determination of plastic constitutive properties of microparticles through single particle compression, Adv. Powder Technol. 26 (2015) 1544–1554.
[22] H. Assadi, F. Gärtner, Particle compression test: A key step towards tailoring of feedstock powder for cold spraying, Coatings. 20 (2020) 458.
[23] KSS Kinetic Spray Solutions GmbH, http://www.kinetic-spray-solutions.com/ (accessed on 2021.04.25).
[24] D. Kwon, H. Park, S. Ghosh, C. Lee, Recrystallization of the copper films deposited by pulsed electroplating on ECR plasma-cleaned copper seed layers, J. Korean Phys. Soc. 44 (2004) 1108–1112.
[25] T. Stoltenhoff, C. Borchers, F. Gärtner, H. Kreye, Microstructures and key properties of cold-sprayed and thermally sprayed copper coatings, Surf. Coat. Technol. 200 (2006) 4947–4960.
[26] C. Borchers, F. Gärtner, T. Stoltenhoff, H. Kreye, Formation of persistent dislocation loops by ultra-high strain-rate deformation during cold spraying, Acta Mater. 53 (2005) 2991–3000.
[27] F.D. Torre, R. Lapovok, J. Sandlin, P.F. Thomson, C.H.J. Davies, E.V. Pereloma, Microstructures and properties of copper processed by equal channel angular extrusion for 1–16 passes, Acta Mater. 52 (2004) 4819–4832.
[28] J. Kusnierz, Rolling texture of ECAP processed Al and Cu, Solid State Phenom. 105 (2005) 339–344.
[29] C. Borchers, F. Gärtner, T. Stoltenhoff, H. Assadi, H. Kreye, Microstructural and macroscopic properties of cold sprayed copper coatings, J. Appl. Phys. 93 (2003) 10064–10070.